photonics

Article

MWIR Meanderline Reflective Quarter-Wave Plate

Bhanu Ghimire and Glenn D. Boreman *

Department of Physics and Optical Science, University of North Carolina at Charlotte, Charlotte, NC 28223, USA; bghimire@charlotte.edu
* Correspondence: gboreman@charlotte.edu

Abstract

We present, for the first time, a design and measured data for a meanderline reflective quarter-wave plate suitable for operation in the 3- to 5-micron MWIR band. Across this spectral range, the reflection coefficient is around 80%, the axial ratio is less than 2, and the polarization conversion ratio is above 75%. We also demonstrate experimentally that the meanderline structure has stable performance as a reflective quarter-wave plate over a 20-degree angular bandwidth centered around incident angles between 35 and 55 degrees. One notable difference as compared to LWIR meanderline waveplates is that the vertical height of the grid lines is necessarily larger, to keep the relative phase between TE and TM near 90°.

Keywords: quarter wave plate; polarization; infrared

1. Introduction

There is continuing interest in metamaterial-based waveplates as an alternative to crystalline waveplates, because crystalline waveplates are comparatively bulky and operate over restricted angular and wavelength bandwidths. Metamaterial-based waveplates are compact and can be easily integrated into optical systems, even in situations of broadband imaging and non-collimated radiation. The infrared band has several applications where polarization-resolved imagery is valuable, including circular dichroism spectroscopy [1], detection of disturbed earth [2], and detection of man-made objects obscured by foliage [3].

Recent metamaterial waveplate research in the mid-wave infrared (MWIR) band of 3–5 μm wavelength has produced designs [4] with measured reflectance above 85% and a predicted stable differential phase shift between TE and TM radiation in the 2.5–3.8 μm range. A polarization conversion efficiency of around 80% over the 3.8–4.8 μm range has been experimentally verified [5]. Additional MWIR modeling [6] has indicated significant potential of reflective metal/dielectric designs as efficient quarter- and half-wave plates.

In our investigations, a metallic meanderline waveplate design allows for a tailored phase shift between TE and TM radiation since current induced along the metallic lines gives an inductive impedance, while the proximity of adjacent metallic lines gives a capacitive impedance. Adjustment of the dimensional variables in the meanderline yields a phase shift near 90 degrees to be obtained on reflection, for efficient linear-to-circular polarization conversion.

We demonstrate for the first time a reflective meanderline-based quarter-wave plate suitable for operation in the mid-wave infrared (MWIR) band of 3–5 microns. Previous work has demonstrated meanderline designs for the long-wave infrared (LWIR) band of 8–12 microns, with both transmissive [7,8] and reflective [9] waveplates demonstrated. In

Check for updates

Received: 21 November 2025
Revised: 5 January 2026
Accepted: 6 January 2026
Published: 16 January 2026

 https://doi.org/10.3390/photonics13010078

general, axial ratios under 2 were obtained across the LWIR, with band-averaged reflectivity around 70% and polarization conversion ratios (PCRs) over 85% for reflective LWIR waveplates. The change in design wavelength for the structure can be accommodated by scaling the geometry proportionally to the wavelength ratio, which produced a starting design. However, differing material properties between MWIR and LWIR require other changes in the design for optimum performance. For MWIR operation, the height of the meanderline grid was found to be a useful design variable in achieving the desired phase shift between transverse electric (TE) and transverse magnetic (TM) waves.

2. Waveplate Design

2.1. Design Trends

Our objective is to determine the desired dimensions and to predict the functionality of a reflective meanderline quarter-wave plate for the MWIR band. The structure is expected to produce a relative phase shift between TE and TM field components of approximately 90° on reflection, with the goal of efficient conversion of linear polarization into circular polarization at MWIR by reflection from the meanderline. We analyzed these structures using HFSS (Ansys Electronics Desktop 2023 R1) finite-element electromagnetic simulation software. A Floquet port was used to align incident TE and TM radiation parallel and perpendicular to the meanderline grid axes. This produced periodic planar structures based on the unit cell shown in Figure 1, which illustrates the radiation's nominal 45° angle of incidence with respect to the meanderline normal, consistent with the use of the structure as a reflective quarter-wave plate. Design optimization was carried out using the Newtonian gradient method included in HFSS. A standard silicon (Si) wafer was used to provide structural support for the reflective meanderline design shown in Figure 1.

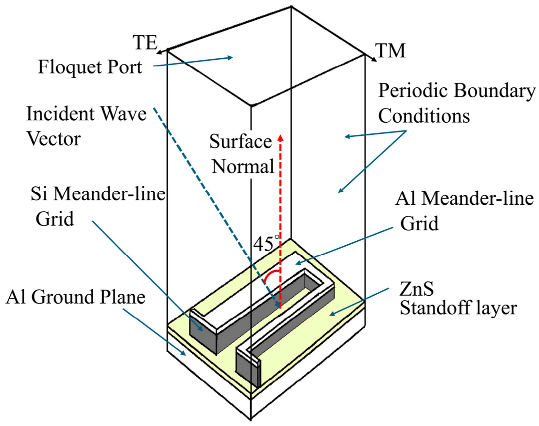

Figure 1. Meanderline unit cell design in HFSS.

The ground plane was aluminum (Al), over which a standoff layer of zinc sulfide (ZnS) was deposited. The meander grid itself was a combination of Si topped by Al. Measured frequency-dependent real and imaginary parts of the dielectric function of the materials used in the modeling were obtained from [10]. We chose initial geometric parameters for a reflective MWIR quarter-wave plate based on the previously published LWIR reflective waveplate design [9], scaled by the ratio of wavelengths. Refinement of the design proceeded with the goals of a 90° phase difference on reflection between TE and TM field components and a high, near-equal reflectivity for both, across the MWIR band.

The LWIR reflective waveplate design [9] used a meander grid composed of 60 nm thick Al on a 650 nm ZnS standoff layer over an Al ground plane. However, for MWIR designs, a meanderline has a smaller capacitive reactance ($X_c = \frac{1}{\omega C}$) than at LWIR because of the higher frequency of operation. As seen in Figure 2, this makes the TE reflected phase almost constant at around 160°. The best design option is then to increase the inductive reactance of the grid, which will modify the TM reflected phase, allowing for the desired phase difference between TE and TM. One way to increase inductive reactance is to increase the current flow in the metallic grid by making the metal lines thicker, lowering their impedance. During the optimization process, an appropriate thickness of Al was estimated to be around 250–300 nm. However, a metallic layer of this thickness is challenging to implement in a conventional lift-off lithographic approach. To avoid this potential fabrication difficulty, we developed the grid design seen in Figure 1, for which the meander grids are constructed from a Si/Al combination, with a chosen design of 100 nm of Al on top of 250 nm of Si. This choice is advantageous because Si has high permittivity at MWIR and thus will confine electric fields inside the grid. The total current induced in the layered structure includes both displacement current in the dielectric and free-electron current in the metal. A convenient and functional design variable is the thickness of the Si meander grids. In Figure 2, we see the computed reflected phase for TE and for TM as a function of grid height h over the 3–5 µm band. In the plot, we assume a 100 nm Al layer on top of the Si. The modeling shows that for TM, there is a dependence of reflected phase on the height of the grid that we can use to achieve the desired 90° phase difference, defined as $\delta = \phi_{TE} - \phi_{TM}$.

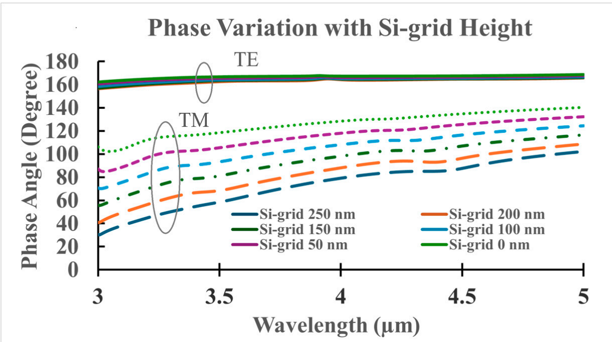

Figure 2. Plot of computed reflected phase for TE and for TM as a function of grid height h and wavelength.

The materials chosen for the design do not exhibit a magnetic response at MWIR frequencies, so the effective index for either TE or TM waves is caused mainly by electric field interactions, characterized by the effective permittivity ($\epsilon_{eff.}$), where $n_{eff} = \sqrt{\epsilon_{eff.}}$. By analogy to classical birefringent waveplates of thickness h [11], the phase delay between TE and TM is given by $\delta = \frac{2\pi\ \Delta n\ h}{\lambda}$ and can be written in terms of permittivity and grid height (h) as

$$\delta = 2 \times \frac{2\pi}{\lambda} \times \mathrm{h}\,(\sqrt{\epsilon_{eff,TE}} - \sqrt{\epsilon_{eff,TM}}) \approx \frac{\pi}{2} \tag{1}$$

where the factor of 2 accounts for the fact that the structure operates in reflection. We numerically investigated the height of the standoff layer on both the phase delay and the reflectivity, with results shown in Figure 3. Based on this modeling, we decided on a ZnS thickness of 110 nm.

We also investigated the choice of metals on reflectivity and the polarization conversion ratio (PCR), as shown in Figure 4. The reflectivity was best in the MWIR for Al. The PCR did not exhibit significant variation with different metal choices. The main issues relating to the choice of materials for a reflective waveplate design are having low absorption loss in the standoff layer, good field concentration in the dielectric portion of the meander grids, and low loss in the metals. We decided to use ZnS as the standoff layer owing to its good transmittance in the MWIR and its availability in our processing facility. The choice of Si for the meander grid was made because of its low loss in the MWIR and

https://doi.org/10.3390/photonics13010078

its relatively high refractive index, facilitating field confinement under the metallic grids. Aluminum was chosen as the metallic portion of the meander grid and for the ground plane because we have measured Al to have better reflectance than gold in the MWIR [10]. Other combinations of materials having similar characteristics may also be suitable design choices.

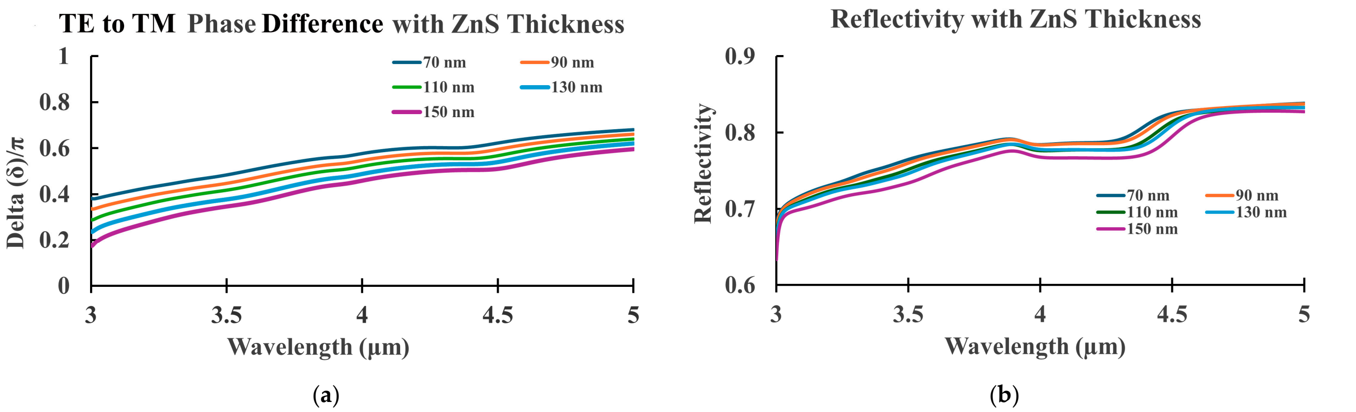

Figure 3. Simulated results from HFSS showing: (**a**) TE to TM phase shift and (**b**) reflectivity as a function of dielectric layer thickness.

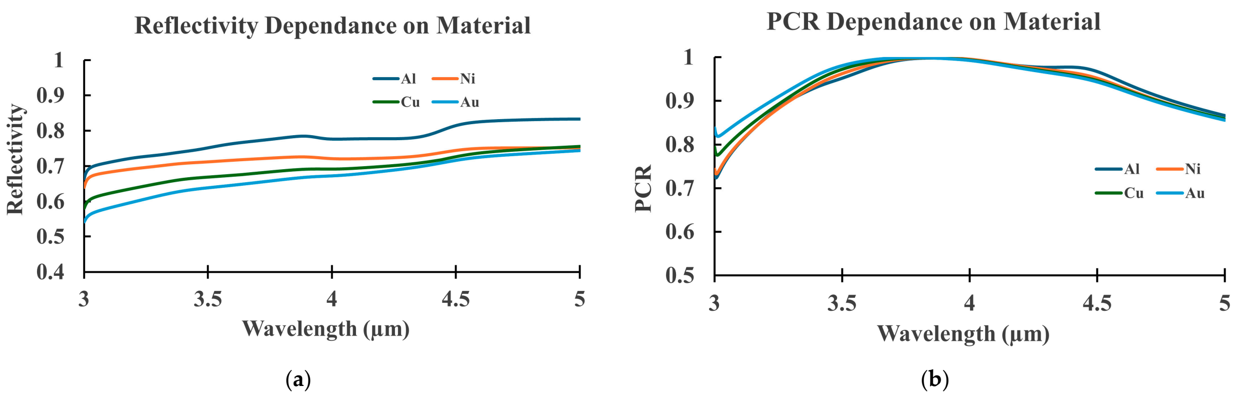

Figure 4. Simulated grid line material performance analysis with HFSS in terms of: (**a**) reflectivity; (**b**) polarization conversion ratio.

2.2. Optimized Design Chosen for Demonstration

In the optimization and modeling, the meander grids were designed as stacked layers of Si (250 nm) and Al (100 nm) developed on a ZnS dielectric standoff layer (110 nm). The design is defined by several geometric parameters as shown in Figure 5: $L = 8.91$ µm, $L' = 8.51$ µm, $l = 8.38$ µm, $\Delta g = 0.45$ µm, $\Delta W = 0.3$ µm, $\Delta w = \Delta b = 0.13$ µm, $b = 0.45$ µm. Each unit cell in the design was thus 8.51 µm × 1.43 µm, and the entire fabricated structure was 5 mm × 5 mm.

The incident radiation is linearly polarized at an angle of 45° with respect to the meanderline axes, so that incident TE and TM components have equal amplitudes. Typically, meanderlines act as two distinct electrical circuits for incident TE and TM waves. TM radiation induces current in meander grids, contributing to inductance, while the TE radiation encounters a capacitive impedance due to the induced electric field between adjacent meanderline grids [12,13]. This arrangement allows meanderline waveplates to produce a relative phase change between TE and TM components.

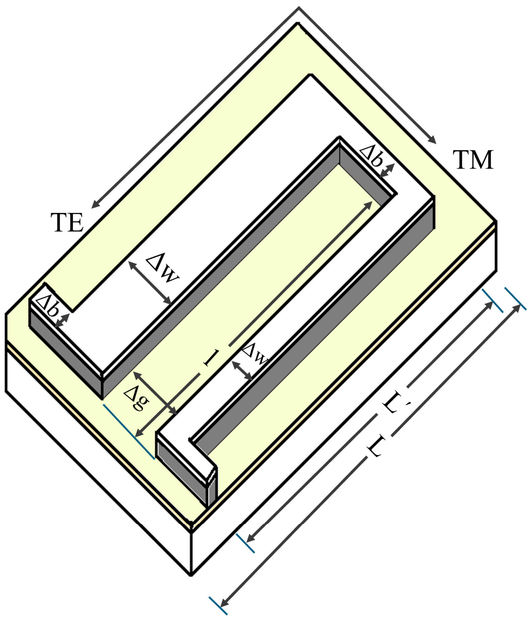

Figure 5. Simulated meander grid geometry.

2.3. Design Figures of Merit

The polarization state of IR radiation can be described by the tilt angle (ψ) and ellipticity (χ) as shown in the polarization ellipse of Figure 6, where

$$\tan\,(2\Psi \pm \frac{\pi}{2}) = \frac{2R_{TE}R_{TM}}{R_{TE}^2 - R_{TM}^2}\cos\delta \tag{2}$$

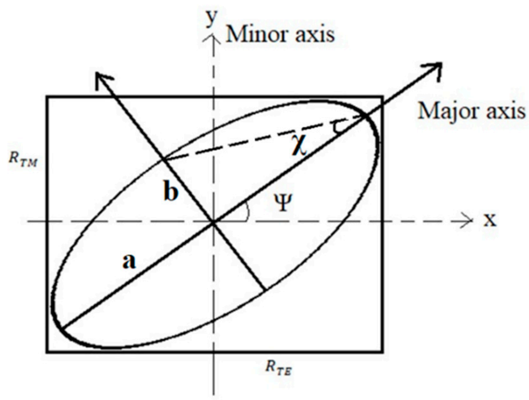

Figure 6. Polarization ellipse.

The factor $\pm\,\pi/2$ differentiates between right and left circular polarization. The axial ratio (AR) is defined as the ratio between the major and minor axes of the elliptically polarized radiation. If the reflected light is circularly polarized, the AR will equal unity [14,15].

$$\mathrm{AR} = \frac{1}{\tan[\frac{1}{2}sin^{-1}(\sin(2\Psi)sin\delta)]} \tag{3}$$

Power reflectivity is the average of power reflectivity R for the TE and TM modes

$$\text{Reflectivity} = \frac{R_{TE} + R_{TM}}{2} \tag{4}$$

The polarization conversion ratio (PCR) is the ratio of the power reflected in the circular polarization state to the total reflected power [16]. The PCR was calculated using power reflection coefficients as

$$PCR = \frac{\left[\sqrt{R_{TE}} - i\sqrt{R_{TM}}e^{i\delta}\right]^2}{2(R_{TE} + R_{TM})} \quad (5)$$

where δ is the phase difference between reflected TE and TM modes. Since the imaginary part of the PCR vanishes for δ = 90°, the real part characterizes the polarization conversion ratio, with the ideal value of unity when the reflection coefficients for TE and TM modes are equal [9].

3. Fabrication

Since operation in MWIR requires small feature sizes, we used electron-beam lithography to define the meander structures. Given the narrow line spacings and the relatively tall meander grid height, the aspect ratios involved indicated the use of reactive ion etching to maintain design parameters. An optically thick Al ground plane was deposited on a Si carrier wafer using an electron-beam deposition system (Lesker PVD-75, Kurt J. Lesker Company, Jefferson Hills, PA, USA). Then, a 110 nm ZnS dielectric standoff layer was deposited on the ground plane using an Edwards 306 vacuum coater (Edwards, Ltd., Burgess Hill, West Sussex, UK). Then, a 250 nm thick Si layer was deposited using an AJA ATC 1800F sputtering tool (AJA International, Hingham, MA, USA). Then, 300 nm of PMMA electron resist was deposited on top of the Si using a spin coater and cured for 120 s using a hotplate at 180 °C. The meander structures were exposed using a Raith 150 electron-beam lithography system (Raith GmbH, Dortmund, Germany). A 100 nm Al mask was e-beam deposited using the Lesker deposition system. Once the desired metallic structure was deposited, the structure was immersed in a N-dimethylacetamide solution for 3 h, and the resist was lifted off using ultrasonic agitation. The meander grids were completed by etching through the 250 nm of sputtered Si using the Al as an etch mask with a Plasma-Therm Versaline deep silicon etcher (Plasma-Therm, LLC, St. Petersburg, FL, USA). This left the meander grids as a combination of 250 nm of Si and 100 nm of Al. An electron micrograph of the completed structure is shown in Figure 7.

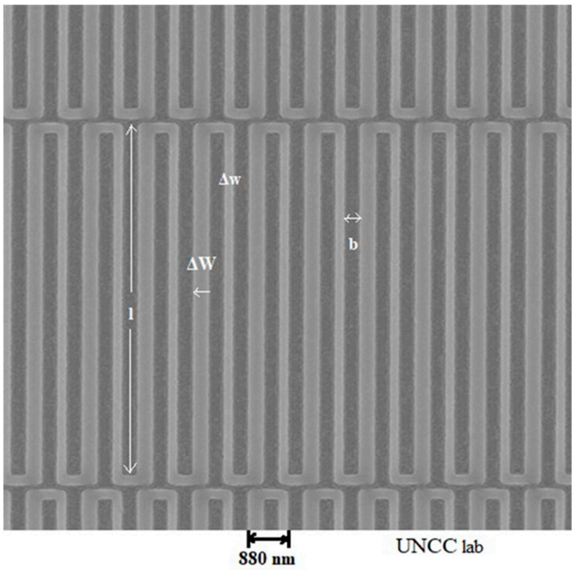

Figure 7. Electron microscope image of the final completed structure.

4. Measurement Results

We measured the waveplate in reflection at a 45° angle of incidence with an IR-VASE infrared ellipsometer (J. A. Woollam Company, Lincoln, NE, USA), which allowed computation of the data shown in Figure 8, according to Equations (1)–(5). The IR-VASE was also used to measure the power reflection coefficient for the two polarizations. In each case, the measured results are shown along with the predicted performance from the HFSS model, over the 3–5 mm band. The reflection coefficient is around 80%, the phase delay δ between TE and TM is close to $\frac{\pi}{2}$, the axial ratio is less than 2, and the polarization conversion ratio is above 75% over the MWIR band. In the plot of reflection coefficient, some low-contrast Fabry–Perot oscillations appear, arising from the layered structure including the ZnS standoff film. The agreement between modeled and measured data is generally within 10%. Possible contributions to these discrepancies may include small differences between designed and as-fabricated dimensions, differences in material properties owing to specific deposition parameters, and measurement uncertainties in the instrumentation.

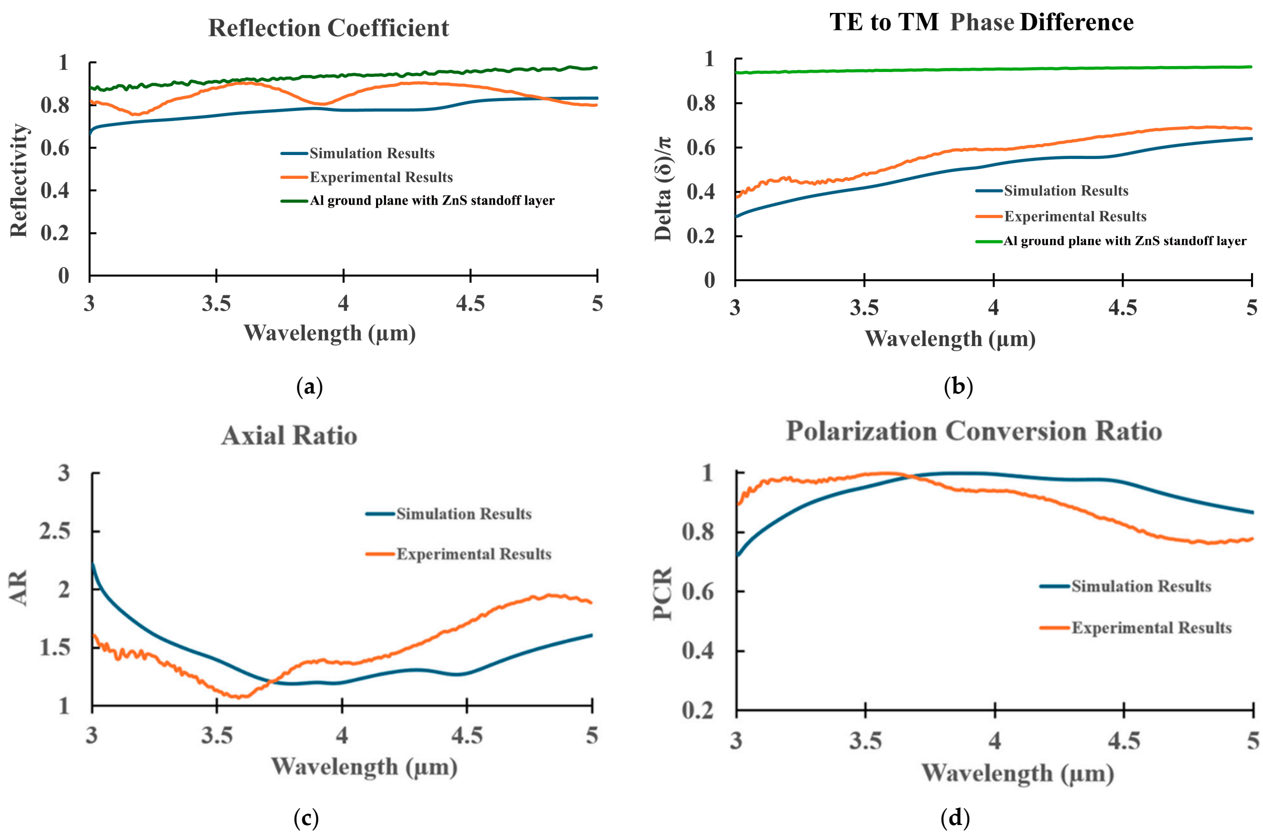

Figure 8. Comparison between modeled and measured IR-VASE ellipsometer data: (**a**) reflection coefficient; (**b**) relative phase difference between TE and TM modes; (**c**) axial ratio; (**d**) polarization conversion ratio.

A radiometric advantage of meanderline waveplates as compared to their crystalline counterparts is that the polarization properties of the structure are relatively insensitive as a function of angle [17]. To verify this behavior, ellipsometry data was acquired for axial ratio and retardance within a 20° angular width for incident angles between 35° and 55°, as shown in Figure 9. The results show that the waveplate operates as expected over a significant angular bandwidth. The waveplate operates as designed for a range of angles around 45 degrees in the plane of incidence perpendicular to the waveplate. For other planes of incidence, the orientation of the electric fields with respect to the structural symmetry of the waveplate is not optimum. For these cases, we have confirmed by modeling that the device performance is degraded, with differential phase between TE and TM showing a considerable range as a function of incidence angle rather than the relatively stable behavior seen in Figure 9b.

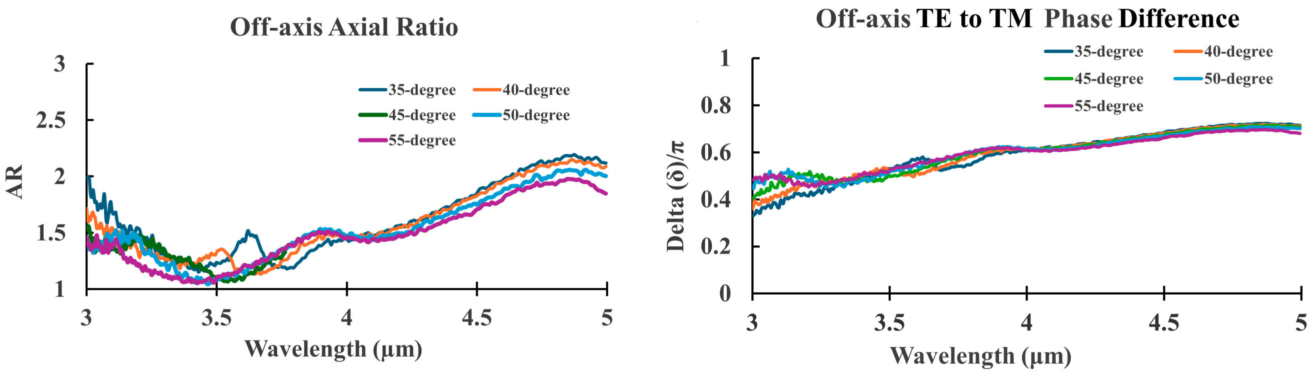

(**a**) (**b**)

Figure 9. Measured data: (**a**) axial ratio; (**b**) phase difference δ within a 20° angular bandwidth centered at angles of incidence from 35° to 55°.

We also measured the Stokes parameters for the waveplate at the 3.39 μm laser wavelength using a Complete Angle Scatter Instrument (CASI, The Scatterworks, Inc., Gresham, OR, USA), which controls the polarization state at both source and receiver. The CASI polarization state generator was fixed, and the polarization state analyzer was rotated at the detector side. The output Stokes parameters were calculated using Mueller matrix elements from incident and reflected beam intensities [18–20].

The output Stokes parameters are

$$\begin{bmatrix} S_0 \\ S_1 \\ S_2 \\ S_3 \end{bmatrix} = \begin{bmatrix} M_{00} & M_{01} & M_{02} & M_{03} \\ M_{10} & M_{11} & M_{12} & M_{13} \\ M_{20} & M_{21} & M_{22} & M_{23} \\ M_{30} & M_{31} & M_{32} & M_{33} \end{bmatrix} \begin{bmatrix} S_0^{in} \\ S_1^{in} \\ S_2^{in} \\ S_3^{in} \end{bmatrix} \tag{6}$$

The output Stokes parameters plotted in Figure 10 were used to calculate the basic polarization parameters of ellipticity (χ), polarization tilt angle (Ψ), and relative phase (δ) between TE and TM modes [1,5].

$$\chi = \frac{1}{2} sin^{-1}(\frac{S_3}{S_0}) \tag{7}$$

$$\Psi = \frac{1}{2} tan^{-1}(\frac{S_2}{S_1}) \tag{8}$$

$$\delta = tan^{-1}(\frac{S_3}{S_2}) \tag{9}$$

The output Stokes parameters calculated using Equation (6) for the waveplate are plotted in Figure 10 for 3.39 μm incident wavelength. It is seen from the diagram that two of the Stokes parameters, S_1 and S_2, are very small, and since $S_1 < 0$ and $S_2 < 0$ for all incident angles, light is more polarized towards the vertical direction, and the preponderance of light is polarized towards the 135° diagonal axis. With this small elliptical distortion, it is evident that the semi-major axis of the polarization ellipse of the reflected beam lies in the second quadrant (90° − 135°). Further, $S_0 \approx S_3 \approx 1$ verifies that the fabricated structure converts a linear polarized beam into right-hand circular polarization in reflection mode.

https://doi.org/10.3390/photonics13010078

The degree of polarization (DOP) was measured in the range from 0.92 to 0.97 in the scatterometer experiments.

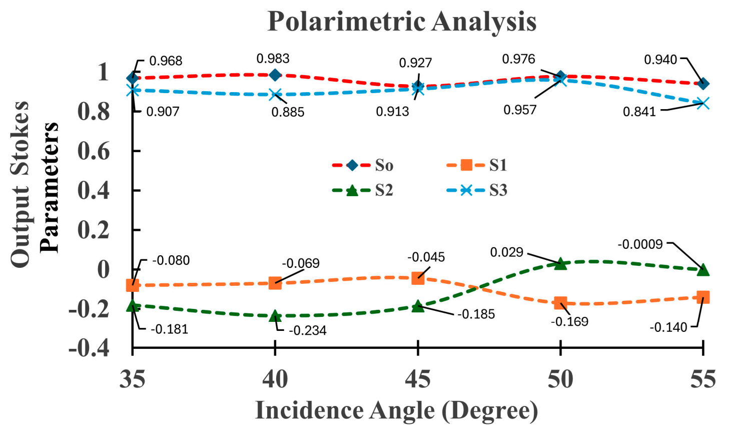

Figure 10. Output Stokes parameters measured at 3.39 μm wavelength using the CASI scatterometer.

Using the CASI, we measured the complete Mueller matrix elements for the waveplate at various angles of incidence. The results are shown in Figure 11. M_{00} represents total normalized output, $M_{30} > 0$ suggests a slight RCP polarization bias with a small chiral effect, large values for M_{31} and M_{32} suggest a strong linear to circular conversion, and $M_{33} > 0$ shows a preference for right-circular polarization in the reflected beam.

1
0.018867925
0.009433962
0.977987421

a) Normalized Stokes Input

1	−0.370303	0.152692	−0.026515
0.376752	−0.759996	−0.323407	−0.449913
−0.127405	0.353639	−0.674949	−0.055254
0.037905	−0.403778	−0.29927	0.900338

b) Mueller matrix elements for 35-degree

1.000000	−0.366016	0.099370	−0.010556
0.364499	−0.812874	−0.364105	−0.424915
−0.113044	0.373470	−0.837242	−0.123802
0.072968	−0.393751	−0.294668	0.841242

c) Mueller matrix elements for 40-degree

1.000000	−0.375006	0.093345	−0.067711
0.350863	−0.870350	−0.392962	−0.384478
−0.107774	0.392255	−0.837180	−0.078732
0.156268	−0.417123	−0.328686	0.785450

d) Mueller matrix elements for 45-degree

1.000000	−0.154809	−0.052437	−0.020277
0.181702	0.192203	−0.910347	−0.354298
−0.157658	0.684772	0.352889	0.175137
0.076348	−0.270934	−0.344808	0.909327

e) Mueller matrix elements for 50-degree

1.000000	−0.155723	−0.061872	−0.057369
0.173031	0.203646	−0.884600,	0.316224
−0.163686	0.674930	0.264198	0.150821
0.020884	−0.239501	−0.378528	0.847137

f) Mueller matrix elements for 55-degree

Figure 11. Mueller matrices for the waveplate measured at angles between 35° and 55°.

A comparison between the IR-VASE and the CASI measurements of the tilt angle, retardance, axial ratio, and polarization conversion ratio over the range of incident angles between 35° and 55° is shown in Figure 12, along with the computed results from simulation. The experimental results from both measurements agree within about 10%.

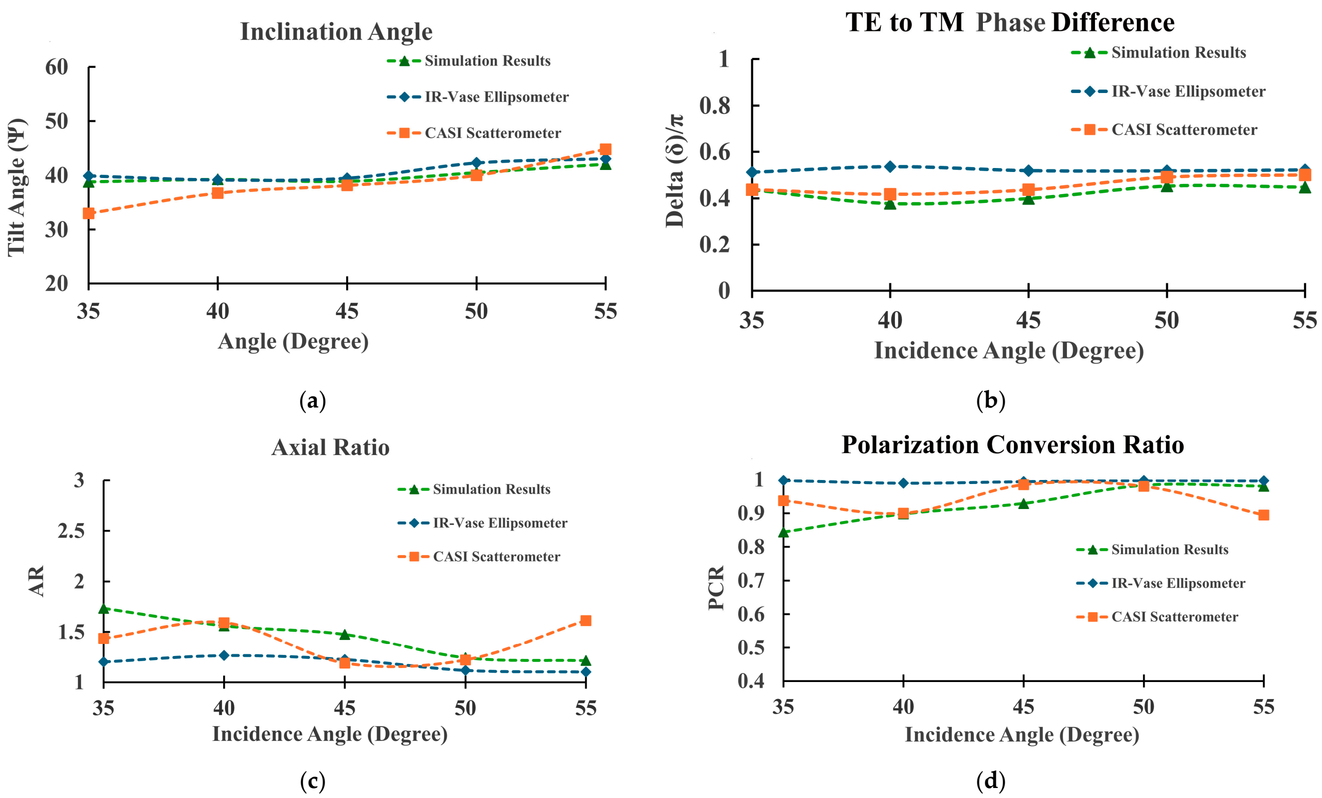

Figure 12. Comparison of ellipsometric and CASI scatterometer experimental data using λ = 3.39 μm for incident angles ranging from 35° to 55°: (**a**) tilt angle of polarization ellipse; (**b**) phase retardance; (**c**) axial ratio; (**d**) polarization conversion ratio.

5. Conclusions

We have presented, for the first time, a design and measured data for a meanderline reflective quarter-wave plate suitable for operation in the MWIR band. The reflection coefficient is around 80%, the phase delay between TE and TM is close to 90°, the axial ratio is less than 2, and the polarization conversion ratio is between 75 and 100% over the MWIR band. The agreement between modeled and measured data is generally within 10%. We also demonstrated via measurements that the meanderline structure has stable performance as a quarter-wave plate over a range of incident angles. One notable difference as compared to LWIR meanderlines is that the height of the grid lines needs to be increased to incur more inductive impedance that keeps the relative phase between TE and TM near 90°.

Author Contributions: Conceptualization, B.G. and G.D.B.; methodology, B.G. and G.D.B.; validation, B.G. and G.D.B.; data curation, B.G. and G.D.B.; formal analysis, B.G. and G.D.B.; visualization, B.G. and G.D.B.; writing—original draft preparation, B.G. and G.D.B.; writing—review and editing, G.D.B.; project administration, G.D.B.; funding acquisition, G.D.B.; supervision, G.D.B.; resources, G.D.B. All authors have read and agreed to the published version of the manuscript.

Funding: This research was funded by the Center for Optical Communications and Optoelectronics at the University of North Carolina at Charlotte.

Data Availability Statement: Data supporting the reported results is available from the corresponding author upon reasonable request.

Acknowledgments: The authors acknowledge experimental assistance from the Center for Optical Communications and Optoelectronics at the University of North Carolina at Charlotte.

Conflicts of Interest: The authors declare no conflicts of interest.

References

1. Yoo, S.; Park, Q. Nanophotonic chiral sensing: From principles to practice. *Photonics Insights* **2025**, *4*, R08. [CrossRef]
2. Petersson, H.; Gustafsson, D. Multi-spectral texture analysis for IED detection. *Proc. SPIE* **2016**, *9988*, 99880P.
3. Brown, J.; Wagner, M.; Roberts, R.; Card, D. Experiments in detecting obscured objects using longwave infrared polarimetric passive imaging. *Proc. SPIE* **2019**, *11001*, 1100107.
4. Jiang, S.; Xiong, X.; Hu, Y.-S.; Hu, Y.-H.; Ma, G.; Peng, R.; Sun, C.; Wang, M. Controlling the polarization state of light with a dispersion-free metastructure. *Phys. Rev. X* **2014**, *4*, 021026. [CrossRef]
5. Zou, H.; Nash, G. Efficient mid-infrared linear-to-circular polarization conversion using a nanorod-based metasurface. *Opt. Mater. Express* **2022**, *12*, 4565–4573. [CrossRef]
6. Abouelatta, M.; Obayya, S.; Hameed, M. Highly efficient transmissive metasurface for polarization control. *Opt. Quantum Electron.* **2021**, *53*, 87. [CrossRef]
7. Tharp, J.; Lopez-Alonso, J.; Ginn, J.; Middleton, C.; Lail, B.; Munk, B.; Boreman, G. Demonstration of a single-layer meanderline phase retarder at infrared. *Opt. Lett.* **2006**, *15*, 2687–2689. [CrossRef] [PubMed]
8. Tharp, J.; Lail, B.; Munk, B.; Boreman, G. Design and demonstration of an infrared meanderline phase retarder. *IEEE Trans. Antennas Propag.* **2007**, *55*, 2983–2988. [CrossRef]
9. Wadsworth, S.; Boreman, G. Broadband infrared meanderline reflective quarter-wave plate. *Opt. Express* **2011**, *19*, 10604–10612. [CrossRef] [PubMed]
10. Folks, W.; Ginn, J.; Shelton, D.; Tharp, J.; Boreman, G. Spectroscopic ellipsometry of materials for infrared micro-device fabrication. *Phys. Status Solidi* **2008**, *5*, 1113–1116. [CrossRef]
11. Collett, E. *Field Guide to Polarization*, 3rd ed.; SPIE Press: Bellingham, WA, USA, 2005; pp. 7–30.
12. Munk, B. *Frequency Selective Surfaces*; Wiley-Interscience: Hoboken, NY, USA, 2000; pp. 19–21.
13. Pang, Y.; Gordon, R. Metal nano-grid reflective wave plate. *Opt. Express* **2009**, *17*, 2871–2879. [CrossRef] [PubMed]
14. Wadsworth, S.; Boreman, G. Comparison of quarter-wave retarders over finite spectral and angular bandwidths for infrared polarimetric-imaging applications. *Appl. Opt.* **2011**, *50*, 6682–6688. [CrossRef] [PubMed]
15. Wadsworth, S.; Boreman, G. Analysis of throughput for multilayer infrared meanderline waveplates. *Opt. Express* **2010**, *18*, 13345–13360. [CrossRef] [PubMed]
16. Gong, Y.; Zhang, Z.; Tang, J.; Ma, L.; Pang, K. Research progress on terahertz achromatic broadband polarization wave plates. *Opt. Laser Technol.* **2023**, *166*, 109633. [CrossRef]
17. Tharp, J.; Alda, J.; Boreman, G. Off-axis behavior of an infrared meander-line waveplate. *Opt. Lett.* **2007**, *32*, 2852–2854. [CrossRef] [PubMed]
18. Goldstein, D. *Polarized Light*, 3rd ed.; CRC Press: Boca Raton, FL, USA, 2017; pp. 725–733.
19. Azzam, R. Stokes-vector and Mueller-matrix polarimetry. *J. Opt. Soc. Am. A* **2016**, *33*, 1396–1408. [CrossRef] [PubMed]
20. Hilfiker, J.; Hong, N.; Schoeche, S. Mueller matrix spectroscopic ellipsometry. *Adv. Opt. Technol.* **2022**, *11*, 59–91. [CrossRef]

https://doi.org/10.3390/photonics13010078